Nat. Hazards Earth Syst. Sci. Discuss., 1, 1799–1822, 2013
www.nat-hazards-earth-syst-sci-discuss.net/1/1799/2013/
doi:10.5194/nhessd-1-1799-2013

Natural Hazards and Earth System Sciences
Open Access
Discussions

Pre-, co-, and post-rockslide analysis with ALOS/PALSAR imagery: a case study of the Jiweishan rockslide, China

C. Zhao[1,2], Q. Zhang[1,2], Y. Yin[3], Z. Lu[4], C. Yang[1,2], W. Zhu[5], and B. Li[6]

[1]College of Geology Engineering and Geomatics, Chang'an University, Xian, Shaanxi 710054, China
[2]Key Laboratory of Western China's Mineral Resources and Geological Engineering, Ministry of Education, No. 126 Yanta Road, Xian, Shaanxi 710054, China
[3]China Geological Survey, 45 Fuwai Dajie, Xicheng District, Beijing 100037, China
[4]US Geological Survey, Vancouver, Washington, USA
[5]Department of Land Surveying and Geo-Informatics, Hong Kong Polytechnic University, Hong Kong, China
[6]Institute of Geomechanics, Chinese Academy of Geological Sciences, Beijing 100081, China

Received: 14 April 2013 – Accepted: 21 April 2013 – Published: 3 May 2013

Correspondence to: C. Zhao (zhaochaoying@163.com)

Published by Copernicus Publications on behalf of the European Geosciences Union.

Abstract

On 5 June 2009, a catastrophic rockslide debris flow occurred at the crest of the Jiweishan range, Chongqing Municipality, China, killing 74 people and injuring an additional eight. We use L-band ALOS/PALSAR imagery to address landslide processes before, during and after the slide. We employ three different SAR methods, i.e. short baseline subsets (SBAS) interferometric SAR (InSAR), SAR backscattering intensity change, and InSAR stacking algorithm, to study any ground deformation before the rockslide, investigate the affected area, and calculate the topographic change by this slide, respectively. First, continuous deformation has been observed based on the available ALOS/PALSAR InSAR imagery during June and December 2007. Second, the area affected by the landslide can be inferred based on changes in SAR backscattering intensity as well as surface topography, with an estimated area of 0.47 million m^2. Last, an InSAR-derived post-slide digital elevation model has allowed us to estimate surface height changes due to the slide, reaching about −80 m at the source region and about 60 m in the deposit region, respectively. Our InSAR-derived estimates have been validated using in-situ data and 3-D LiDAR measurements. The proposed procedures for rockslide analysis with satellite SAR imagery over a remote, mountainous, heavily vegetated region can be further extended to similar geo-hazards investigation and monitoring.

1 Introduction

Rockslide is the movement of a mass of rock, debris, or earth down a slope under the influence of gravity (Cruden and Varnes, 1996). Rockslide failures have resulted in enormous casualties and huge economic losses in mountainous regions (Kwong et al., 2004; Parker et al., 2011; Xu et al., 2010). In recent years, many different mapping techniques have been implemented to study rockslide inventories, deformation monitoring, and hazard and vulnerability assessments (Parise, 2001). In order to achieve

NHESSD
1, 1799–1822, 2013

the best results, both conventional methods such as geomorphological field mapping, visual interpretation of aerial photographs and new techniques such as interpretation and analysis of satellite imagery are frequently applied (Guzzetti et al., 2012).

Satellite synthetic aperture radar (SAR) has great advantages due to its broad coverage and high spatial resolution under all weather conditions (Massonnet and Feigl, 1998). Interferometric SAR (InSAR) technique has been used in various landslide studies, not only for location detection (Cascini et al., 2010; Bulmer et al., 2006; Zhao et al., 2012a), but also for deformation monitoring. Various InSAR techniques have been employed, including the traditional differential InSAR method (Strozzi et al., 2005), the short baseline subsets (SBAS) InSAR method (Berardino et al., 2003), the corner reflector InSAR (Fu et al., 2010; Xia et al., 2004), the persistent scatterer InSAR technique (Hilley et al., 2004; Colesanti et al., 2003; Vladimir and Jan, 2011) and ground based InSAR technique (Leva et al., 2003). InSAR-derived landslide deformation patterns further provide insights into the dynamics of landslides, including the interaction of landslides and tectonic motions and the deformation characteristics in relation to the El Nino phenomenon (Hilley et al., 2004; Colesanti et al., 2003) and the precipitation rate (Zhao et al., 2012a). In addition, InSAR can be used to calculate a digital elevation model (DEM) and therefore calculate topographic changes induced by a landslide (e.g. Lu et al., 2010). Furthermore, the change in SAR backscattering intensity can be used to infer the area affected by a landslide (Lu et al., 2010). The challenges in the application of the InSAR technique to landslide investigation are due to the vegetation and temporal decorrelation as well as atmospheric delay anomalies (Zebker and Villasenor, 1992; Berardino et al., 2003). Also, the side-looking SAR imaging geometry can cause layover and shadow defects in mountainous regions.

The Jiweishan rockslide debris flow occurred at the crest of the Jiweishan, Chongqing Municipality, China, where an iron mine is located (Fig. 1). According to the classification of rockslide by Hungr et al. (2001), the Jiweishan rockslide can be classified as a rockslide debris flow. The Jiweishan range elongates along the N–S direction. The eastern flank of the range is a 50 ~ 150 m cliff facing towards Tiejiang

NHESSD
1, 1799–1822, 2013

creek to the east. The terrain over the Jiweishan varies from 1442 m a.s.l. at the peak to 1000 m a.s.l. at the toe, giving a height difference of about 440 m. The rock movement can be traced back to 1960s, when a crack was found on the surface of the east-facing cliff. In 1999, the width of the crack reached 1.5 m (Xu et al., 2010). In September 2001, some small-scale rockfalls occurred in the southern part of the cliff. After 2005, the rock fall activity increased and began to extend to the northern part of the cliff progressively. In July and August 2007, geo-hazard investigation of the Jiweishan was carried out by a professional geological team (Xu et al., 2010; Yin et al., 2011). A rock avalanche zone along the eastern cliff, about 1000 m long, 10 m wide, and 15–20 m high (a volume of about 200 000 m^3), was defined. The eastern boundary of the potential affected area is accompanied by Tiejiang creek at the foot of the mountain. People in the potential affected area were evacuated. However, at that time nobody predicted that such a large and high speed rockslide would occur in the Jiweishan, due to the limited understanding of the complex geomorphology and the historical activity of the slide. Unfortunately, at about 3 p.m. on 5 June 2009, an approximately five-million cubic meter rock mass slid along the weak interlayer. Rock mass from the source area (the southern part of the Jiweishan) disintegrated quickly and dropped more than 50 m of debris into Tiejiang creek. Because of the huge kinetic energy, the sliding mass rode over the valley and ran up the opposite slope of Tiejiang creek. Blocked by this slope, the slide mass transformed into a high-speed debris flow, which travelled down along Tiejiang creek and formed an about 2.2 km long deposit. An ore mine was obliterated, with a loss of 74 persons. It was estimated that the whole sliding process lasted less than 1 min (Xu et al., 2010).

To investigate this huge catastrophic rockslide avalanche (fragment flow), multiple methods including field investigation, remote sensing (except SAR imagery data), 3-D LiDAR and aerial photographs taken by an unmanned airplane were used (Xu et al., 2010; Yin et al., 2011). In this study, we employ satellite SAR imagery to recover the pre-slide time-series deformation, co-slide affected area and post-slide height change. We arrange this manuscript as follows: Sect. 2 gives the SAR data and research

NHESSD
1, 1799–1822, 2013

schemes; Sect. 3 introduces the methods involved; Sect. 4 contains the results and analysis; and the last section provides some concluding remarks.

2 Data and research schemes

The Jiweishan mountainous region is located in the southwest of China, where the topographic relief is over 400 m. The foggy and rainy climate has made it impossible to obtain optical satellite imagery, and flourishing vegetation decorrelates InSAR imagery at shorter wavelengths. L-band advanced land satellite observation (ALOS) PALSAR data has more advantages than C-band Envisat and X-band TerraSAR-X data due to its longer wavelength (e.g. Lu et al., 2010). Accordingly, we have obtained archived ALOS/PALSAR data over the study area: a total of 11 scenes of ALOS/PALSAR data are applied. A 3-arc-second SRTM DEM (http://srtm.csi.cgiar.org) is used for both differential InSAR deformation mapping and DEM change calculation. In order to get high-spatial deformation images, the fine beam double polarization (FBD) images are oversampled to the pixel spacing of the fine beam single polarization (FBS) images. Moreover, only a multi-look number of 2 (1 pixel in the range and 2 pixels in the azimuth directions) is applied to generate InSAR interferograms at a spatial spacing of ~ 7.5 m in both directions. Images at this spacing have the potential to detect small-scale rockslides and also are better suited to map rockslides with large deformation gradients at the expense of low coherence (Sandwell et al., 2008).

Our objectives are to (1) investigate any landslide motion before the catastrophic collapse, (2) infer the area affected by the landslide, and (3) estimate topographic changes caused by the landslide. Accordingly, we generate the following 3 groups of interferograms (Fig. 2):

1. 7 interferograms are used to obtain pre-slide deformation time series;
2. 2 closest SAR intensity images spanning the 5 June 2009 rockslide are used to infer the area affected by the rockslide;

NHESSD
1, 1799–1822, 2013

3. 7 interferometric pairs after the rockslide are used to obtain surface height change caused by the rockslide.

3 Methodology

3.1 Pre-rockslide time-series deformation monitoring with SBAS algorithm

In order to mitigate the atmospheric artefacts and the residual topographic effect in multi-temporal InSAR images, one of the advanced InSAR techniques termed as short baseline subsets (SBAS) InSAR technique is applied (Berardino et al., 2002). SBAS also works when limited interferometric sets are available (Mora et al., 2003). Before SBAS calculation, a minimum cost flow unwrapping algorithm (Chen and Zebker, 2002) is used to unwrap the phase in two dimensions and then a phase closure technique (Biggs et al., 2007) was used to identify the major unwrapping errors remaining in the interferograms.

For a given unwrapped interferogram j, the phase at pixel (x, r) (where x and r are the azimuth and slant range coordinates, respectively) computed from the SAR acquisitions at epoch t_A (start time) and t_B (end time) can be written as follows (Berardino et al., 2002):

$$\begin{aligned}\delta\varphi_j(x,r) &= \varphi(t_B,x,r) - \varphi(t_A,x,r) \\ &= \delta\varphi_j^{\text{defo}}(x,r) + \delta\varphi_j^{\text{topo}}(x,r) + \delta\varphi_j^{\text{atm}}(x,r) + \delta\varphi_j^{\text{noise}}(x,r) \end{aligned} \quad (1)$$

where, $\delta\varphi_j^{\text{defo}}$ is slant deformation phase between t_A and t_B; $\delta\varphi_j^{\text{topo}}$ represents topographic phase error, its impact on deformation maps is a function of the perpendicular baseline $B_{\perp j}$, the slant range distance R, look angle θ and DEM error ΔZ; $\delta\varphi_j^{\text{atm}}$ accounts for temporal atmospheric variation at different SAR acquisition t_A and t_B; the final term $\delta\varphi_j^{\text{noise}}$ is the other noise sum. The first three terms of the right side of

NHESSD
1, 1799–1822, 2013

Eq. (1) can be expressed as follows

$$\begin{cases} \delta\varphi_j^{\text{defo}}(x,r) = \dfrac{4\pi}{\lambda}\left[d\left(t_{\text{B}},x,r\right) - d\left(t_{\text{A}},x,r\right)\right] = a_j(x,r)\cdot v + \delta\varphi_j^{\text{nl\_defo}}(x,r) \\ \delta\varphi_j^{\text{topo}}(x,r) = \dfrac{4\pi}{\lambda}\dfrac{B_{\perp j}\Delta Z}{R\sin\theta} = b_j(x,r)\cdot\Delta Z \\ \delta\varphi_j^{\text{atm}}(x,r) = \varphi_{\text{atm}}\left(t_{\text{B}},x,r\right) - \varphi_{\text{atm}}\left(t_{\text{A}},x,r\right) \end{cases} \tag{2}$$

where λ is the SAR wavelength, v is the deformation rate, $\delta\varphi_j^{\text{nl\_defo}}(x,r)$ is the nonlinear deformation between two SAR acquisition dates. The Eq. (1) can then be rewritten in matrix form as follows

$$\delta\varphi(x,r) = [A(x,r),B(x,r)]\begin{bmatrix} v \\ \Delta Z \end{bmatrix} + N(x,r) \tag{3}$$

where $A(x,r) = [a_1(x,r)\ldots a_M(x,r)]^T$, $B(x,r) = [b_1(x,r)\ldots b_M(x,r)]^T$. The estimated linear deformation rate and DEM error phases are then subtracted from all unwrapped interferograms. Next, the atmospheric phase can be separated by high-pass filtering in the temporal domain and low-pass filtering in the spatial domain, because the atmospheric artefacts are spatially correlated and temporally random (Ferretti et al., 2001). If there exit several sub-datasets, a general inverse method such as singular value decomposition (SVD) is applied to estimate the deformation at each SAR acquisition date and DEM error. Then, the nonlinear deformation phase at different SAR acquisition dates will be calculated. Lastly, the accumulated deformation series can be achieved by integrating the deformation in each neighbouring SAR acquisition dates as follows.

$$\delta\varphi_k^{\text{defo}}(x,r) = (t_k - t_1)v + \sum_{i=2}^{k}\phi_i^{\text{nl\_defo}}, \tag{4}$$

where t_1 is the earliest SAR acquisition date, t_k is the k-th SAR acquisition date.

NHESSD
1, 1799–1822, 2013

3.2 Down-slope deformation calculation

InSAR can only measure the deformation along the line-of-light (LOS) direction. That is, the InSAR measurement represents the component of ground deformation projected to the LOS direction. Given some assumptions, the LOS deformation can be transformed to the measurement with a specific angle and azimuth direction. The transformation between the LOS direction and down-slope direction is straight forward. The unit vector of LOS can be defined as follows (Zhao et al., 2012a).

$$\boldsymbol{r} = \begin{bmatrix} r_{\text{east}} \\ r_{\text{north}} \\ r_{\text{up}} \end{bmatrix} = \begin{bmatrix} -\sin\theta\cos\alpha_{\text{s}} \\ \sin\theta\sin\alpha_{\text{s}} \\ \cos\theta \end{bmatrix} \tag{5}$$

where θ is incidence angle with respect to the "flat earth", i.e. the angle between the vertical direction and the radar LOS, and α_{s} is the satellite flight azimuth. The unit vector of slope direction can be defined as follows.

$$\boldsymbol{u} = \begin{bmatrix} u_{\text{east}} \\ u_{\text{north}} \\ u_{\text{up}} \end{bmatrix} = \begin{bmatrix} -\sin\alpha\cos\phi \\ -\cos\alpha\cos\phi \\ \sin\phi \end{bmatrix} \tag{6}$$

where ϕ is the slope angle above the horizontal surface and α is the slope azimuth (aspect angle). So the deformation in the slope direction can be expressed as (Zhao et al., 2012a).

$$d_{\text{slope}} = d_{\text{LOS}} / \left(r_{\text{east}} u_{\text{east}} + r_{\text{north}} u_{\text{north}} + r_{\text{up}} u_{\text{up}} \right) \tag{7}$$

3.3 Co-rockslide affected region detection with SAR intensity map

SAR backscattering intensity is the cumulative contribution of surface roughness, dielectric constant, and terrain slope, all of which are a function of radar parameters such

NHESSD
1, 1799–1822, 2013

as incidence angle, wavelength, and polarization (Ulaby et al., 1986). For the repeat-pass radar observations, the ratio of backscattering intensity qualitatively reflects the change in surface roughness and dielectric constant (which is primarily controlled by surface moisture) (Lu and Meyer, 2002; Lu et al., 2010). Therefore, we delineate the landslide-affected area mainly using the ratio of SAR backscattering returns. However, if the co-event SAR image pair maintains adequate coherence, the loss of coherence of the co-event interferogram can be used to further infer the area affected by the rockslide collapse (Lu et al., 2010).

3.4 Post-rockslide height change calculation

Before the rockslide on 5 June 2009, much of the Jiweishan was covered by heavy vegetation (Fig. 3a), resulting a complete loss of coherence for C-band interferograms. The coherence for L-band interferograms is generally poor and can be lost if the perpendicular baseline is more than about 1 km. However, after the sliding, the vegetation was destroyed (Fig. 3b), making the InSAR images coherent for a long time.

We employ the multi-interferogram method (Ferretti et al., 1999; Lu et al., 2003; Zhao et al., 2012b; Ebmeier et al., 2012) to generate a DEM that represents the surface topography after the rockslide. We produce interferograms with the shortest temporal intervals and mitigate the difficulty in phase unwrapping over the mountainous region by subtracting the 3-arc second SRTM DEM from each interferogram. Then the interferograms are stacked to calculate the final DEM change map.

4 Results and analysis

4.1 Pre-rockslide time-series deformation

The flight direction of ascending ALOS satellite is −10.2 degree from the north and the incidence angle is 38.7 degree from the vertical over the Jiweishan rockslide. The rockslide geometry is defined with the azimuth direction as 12 degree from the north and

NHESSD
1, 1799–1822, 2013

the slope angle as 14.8 degree below the surface (Xu et al., 2010). Accordingly, time-series deformation maps in down-slope direction can be generated with the abovementioned algorithm in Sects. 3.1 and 3.2. Four time-series deformation maps with a time separation of 46 days between adjacent acquisitions are shown in Fig. 4.

From Fig. 4, we can see the obvious deformation phenomena occurred as early as 10 June 2007 and the surface continuously deformed during the monitoring period. Unfortunately, we do not have earlier SAR data to trace the deformation before June 2007. Neither do we have coherent interferograms to allow us to analyze any ground deformation between 11 December 2007 and 5 June 2009. However, we are sure that precursory pre-rockslide time-series deformation exists based on the available interferograms (Fig. 4).

In order to closely analyze the deformation of the Jiweishan before the rockslide, the cumulative deformation during 10 June 2007 and 11 December 2007 is shown in Fig. 5, where the deformed region is outlined and the total deformation (in 184 days) along profile AB is shown in Fig. 6.

Based on Figs. 4 and 5, the deformed part of the Jiweishan, the source of 5 June 2009 debris flow, is obviously distinguishable from the stable part. The length of the deformed block (outlined as an irregular polygon in Fig. 5), is over 600 m. The average width of the deformed block is around 150 m. The deformed geometry can be partially verified with an aerial photograph taken after sliding (shown as inset in Fig. 5). As described by Xu et al. (2010), and Yin et al (2011), the source area of the rockslide can be divided into two parts: a driving block to the south and a resisting block to the north. The driving block is a quasi-quadrilateral shape in plane with a length of 480 m and an average width of 140 m. The resisting block to the north is a triangle shape in plane, with a length of 240 m and an average width of 130 m. So, the pre-slide deformed shape from our InSAR measurement and the sliding shape from the post-slide aerial photo are highly consistent.

As shown from Fig. 6, the deformed length of the Jiweishan slide is over 600 m along the profile AB based on InSAR measurements. There is a difference of around 100 m in

NHESSD
1, 1799–1822, 2013

length between the InSAR and the aerial photograph measurements. This is because the front part (the north part) of the slide is incoherent and no useful deformation can be achieved based on InSAR phase measurements. In addition, InSAR measurements suggest spatially variable deformation patterns along the slide (Fig. 6). The lower elevation part of the slide deformed more than the higher elevation part. The maximum deformation within 184 days amounted to 35 cm in down-slope direction.

4.2 Co-rockslide intensity change map

The two closest SAR images across the rockslide event are used to detect the affected area. The intensity maps acquired on 28 January 2009 and 15 June 2009 are shown in Figs. 7a and b, respectively, while the change map between Figs. 7a and b is shown in Fig. 7c. For comparison, the affected area obtained from aerial photography (Xu et al., 2010) is outlined with the dashed line. Areas with significant changes such as the source region, the scouring region and the deposit region, can be inferred based on SAR intensity changes (Fig. 7c). The source and scouring regions are characterized by lower SAR backscattering returns after the sliding event while the deposit region is marked with higher backscattering after the rockslide. However, we have found that SAR intensity images can not precisely delineate the whole area affected by the rockslide. If we had two SAR images with a shorter time span, we could also explore InSAR coherence change to assist the mapping of the affected area (Lu et al., 2010). Unfortunately, we do not have any adequate interferogram spanning the 5 June 2009 rockslide to allow us to infer the affected area based on coherence loss (Lu et al., 2010).

4.3 Post-rockslide height change estimation

In order to quantitatively assess the affected area and surface damage caused by the rockslide, a height change map (shown in Fig. 8) is generated based on the stacking result from 7 post-slide interferograms.

NHESSD
1, 1799–1822, 2013

From Fig. 8, the affected area can be segmented into three parts: one source part to the south, the scouring area in the middle, and the deposit part to the north. The total length of the affected area is over 2 km and the maximum width of affected area is about 450 m. Even though, there are some incoherent areas caused by layover in the cliff and scouring regions, the height change map detected by InSAR is consistent with the thickness contour map measured by 3-D LiDAR technique (Yin et al., 2011). We validate the DEM change estimated by InSAR using the measurements from 3-D LiDAR technique (Fig. 9).

From Fig. 9, we can conclude that the height and height change are reversely correlated, i.e. the mass slid from the higher elevation part to the lower elevation part. The length of source part is 600 m, and the length of two deposit parts is ~ 1.6 km. The maximum decreased height was around 80 m over the source region and the thickest deposit was about 60 m located at the lower elevation part. The remaining debris entrained and scoured the convex slopes, crossed over Tiejiang creek, rushed up the opposite creek wall and was deposited at a lower elevation for another ~ 30 m. The DEM change profiles from InSAR and 3-D LiDAR measurements agree with each other very well. Please note the InSAR measurement is affected by decorrelation over steep slopes. Ideally this problem can be compensated by InSAR imagery of the opposite viewing geometry if available.

5 Concluding remarks

L-band ALOS/PALSAR imagery data have been successfully used to map three stages of rockslide surface changes, including pre-slide time-series deformation monitoring, co-slide affected region detection and post-slide height change measurement. The co-slide affected area and post-slide height change results are validated with aerial photography and 3-D LiDAR measurements conducted after the rockslide and good agreement is achieved. Most importantly, pre-slide time-series deformation has been recovered with limited available SAR imagery, which can be very useful to study the

NHESSD
1, 1799–1822, 2013

mechanism of the rockslide. Lastly, the methods of investigating this rockslide can also be extended to the other rockslide cases, which will be beneficial to slide early warning and timely protection.

Acknowledgements. ALOS/PALSAR data are copyrighted JAXA/METI and provided by the Alaska Satellite Facility through the ALOS Data Consortium. This research is funded by Natural Science Foundation of China (NSFC) (No: 41072266, 41274005, 41274004) and the Ministry of Land & Resources, China (No: 121201122014).

References

Berardino, P., Fornaro, G., Lanari, R., and Sansosti, E.: A new algorithm for surface deformation monitoring based on small baseline differential SAR interferometry, IEEE T. Geosci. Remote, 40, 2375–2383, 2002.

Berardino, P., Costantini, G., Franceschetti, G., Iodice, L., Pietranera, L., and Rizzo, V.: Use of differential SAR interferometry in monitoring and modeling large slope instability at Matera (Basilicata, Italy), Eng. Geol., 68, 31–51, 2003.

Biggs, J., Wright, T., Lu, Z., and Parsons, B.: Multi-interferogram method for measuring interseismic deformation: Denali fault, Alaska, Geophys. J. Int., 170, 1165–1179, 2007.

Bulmer, M. H., Petley, D. N., Murphy, W., and Mantovani, F.: Detecting slope deformation using two-pass differential interferometry: implications for landslide studies on Earth and other planetary bodies, J. Geophys. Res., 111, E06S16, doi:10.1029/2005JE002593, 2006.

Cascini, L., Fornaro, G., and Peduto, D.: Advanced low- and full-resolution DInSAR map generation for slow-moving landslide analysis at different scales, Eng. Geol., 112, 29–42, 2010.

Chen, C. W. and Zebker, H. A.: Phase unwrapping for large SAR interferograms: statistical segmentation and generalized network models, IEEE T. Geosci. Remote, 40, 1709–1719, 2002.

Colesanti, C., Ferretti, A., Prati, C., and Rocca, F.: Monitoring landslides and tectonic motions with the Permanent Scatterers Technique, Eng. Geol., 68, 3–14, 2003.

Cruden, D. M. and Varnes, D. J.: Landslide types and processes, in: Rockslides, Investigation and Mitigation, Special Report 247, edited by: Turner, A. K. and Schuster, R. L., Transportation Research Board, Washington D.C., 36–75, 1996.

NHESSD

1, 1799–1822, 2013

Ebmeier, S. K., Biggs, J., Mather, T. A., Elliott, J. R., Wadge, G., and Amelung, F.: Measuring large topographic change with InSAR: lava thicknesses, extrusion rate and subsidence rate at Santiaguito volcano, Guatemala, Earth Planet. Sci. Lett., 335, 216–225, 2012.

Ferretti, A., Prati, C., and Rocca, F.: Multibaseline InSAR DEM reconstruction: the wavelet approach, IEEE T. Geosci. Remote, 37, 705–715, 1999.

Ferretti, A., Prati, C., and Rocca, F.: Permanent scatterers in SAR interferometry, IEEE T. Geosci. Remote, 39, 8–20, 2001.

Fu, X., Guo, H., Tian, Q., and Guo, X.: Landslide monitoring by corner reflectors differential interferometry SAR, Int. J. Remote Sens., 31, 6387–6400, 2010.

Greif, V. and Vlcko, J.: Monitoring of post-failure landslide deformation by the PS-InSAR technique at Lubietova in central Slovakia, Environ. Earth Sci., 66, 1585–1595, doi:10.1007/s12665-011-0951-x, 2011.

Guzzetti, F., Mondini, A. C., Cardinali, M., Fiorucci, F., Santangelo, M., and Chang, K. T.: Landslide inventory maps: new tools for an old problem, Earth Sci. Rev., 112, 42–66, 2012.

Hilley, G. E., Burgmann, R., Ferretti, A., Novali, F., and Rocca, F.: Dynamics of slow-moving landslides from permanent scatterer analysis, Science, 304, 1952–1955, 2004.

Hungr, O., Evens, S. G., Bovis, M. J., and Hutchinson, J. N.: A review of the classification of landslides of the flow type, Environ. Eng. Geosci., 7, 221–238, 2001.

Kwong, A. K. L., Wang, M., Lee, C. F., and Law, K. T.: A review of landslide problems and mitigation measures in Chongqing and Hong Kong: similarities and differences, Eng. Geol., 76, 27–39, 2004.

Leva, D., Nico, G., Tarchi, D., Fortuny, G. J., and Sieber, A. J.: Temporal analysis of a landslide by means of a ground-based SAR interferometer, IEEE T. Geosci. Remote, 41, 745–752, 2003.

Lu, Z. and Meyer, D.: Study of high SAR backscattering due to an increase of soil moisture over less vegetated area: its implication for characteristic of backscattering, Int. J. Remote Sens., 23, 1065–1076, 2002.

Lu, Z., Fielding, E., Patrick, M., and Trautwein, C.: Estimating lava volume by precision combination of multiple baseline spaceborne and airborne interferometric synthetic aperture radar: the 1997 eruption of Okmok volcano, Alaska, IEEE T. Geosci. Remote, 41, 1428–1436, 2003.

Lu, Z., Dzurisin, D., Jung, H. S., Zhang, J. X., and Zhang, Y. H.: Radar image and data fusion for natural hazards characterization, Int. J. Image Data Fusion, 1, 217–242, 2010.

NHESSD
1, 1799–1822, 2013

Massonnet, D. and Feigl, K. L.: Radar interferometry and its application to changes in the Earth's surface, Rev. Geophys., 36, 441–500, 1998.
Mora, O., Mallorqui, J. J., and Broquetas, A.: Linear and nonlinear terrain deformation maps from a reduced set of interferometric SAR images, IEEE T. Geosci. Remote, 41, 2243–2253, 2003.
Parise, M.: Landslide mapping techniques and their use in the assessment of the landslide hazard, Phys. Chem. Earth C, 26, 697–703, 2001.
Parker, R. N., Densmore, A. L., Rosser, N. J., de Marcello, M., Li, Y., Huang, R. Q., Whadcoat, S., and Petley, D. N.: Mass wasting triggered by the 2008 Wenchuan earthquake is greater than orogenic growth, Nat. Geosci., 4, 449–52, 2011.
Sandwell, D., Myer, D., Mellors, R., Masanobu, S., Benjamin, B., and James, F.: Accuracy and resolution of ALOS interferometry: vector deformation maps of the father's day intrusion at Kilauea, IEEE T. Geosci. Remote, 46, 3524–3534, 2008.
Strozzi, T., Farina, P., Corsini, A., Ambrosi, C., Thüring, M., Zilger, J., Wiesmann, A., Wegmüller, U., and Werner, C.: Survey and monitoring of landslide displacements by means of L-band satellite SAR interferometry, Landslides, 2, 193–201, 2005.
Ulaby, F. T., Moore, R. K., and Fung, A. K.: Microwave Remote Sensing: Active and Passive, Vol. 3, From Theory to Applications, Artech House, Norwood, Mass., 1097 pp., 1986.
Xia, Y., Kaufmann, H., and Guo, X. F.: Landslide monitoring in the Three Gorges area using D-INSAR and corner reflectors, Photogramm. Eng. Rem. S., 70, 1167–1172, 2004.
Xu, Q., Fan, X. M., Huang, R. Q., Yin, Y. P., Hou, S. S., Dong, X. J., and Tang, M. G.: A catastrophic rockslide-debris flow in Wulong, Chongqing, China in 2009: background, characterization, and causes, Landslides, 7, 75–87, 2010.
Yin, Y. P., Sun, P., Zhang, M., and Li, B.: Mechanism on apparent dip sliding of oblique inclined bedding rockslide at Jiweishan, Chongqing, China, Landslides, 8, 49–65, 2011.
Zebker, A. H. and Villasenor, J.: Decorrelation in interferometric radar echoes, IEEE T. Geosci. Remote, 30, 950–959, 1992.
Zhao, C. Y., Lu, Z., Zhang, Q., and de la Fuente, J.: Large-area landslides detection and monitoring with ALOS/PALSAR imagery data over northern California and southern Oregon, USA, Remote Sens. Environ., 124, 348–359, 2012a.
Zhao, C. Y., Qu, F. F., Zhang, Q., and Zhu, W.: A combined multi-interferogram algorithm for high resolution DEM reconstruction over deformed regions with TerraSAR-X data, J. Geodynam., 61, 148–153, 2012b.

NHESSD
1, 1799–1822, 2013

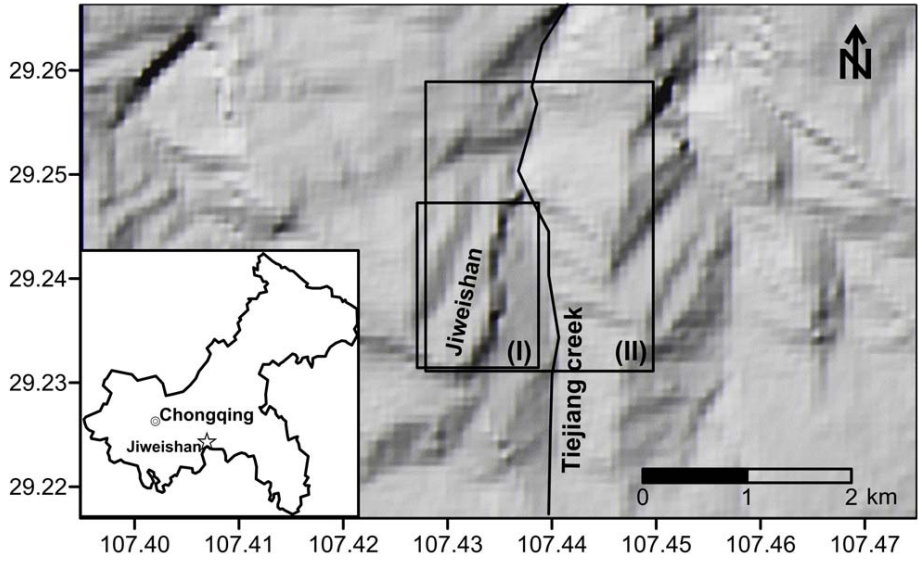

Fig. 1. Shaded-relief image over the Jiweishan range, Chongqing Municipality, China. Two rectangles labelled as (I) and (II) will be further discussed in Figs. 4 and 5 and Figs. 7 and 8, respectively. The inset is a sketch map of Chongqing Municipality, showing the relative location of the Jiweishan range.

NHESSD
1, 1799–1822, 2013

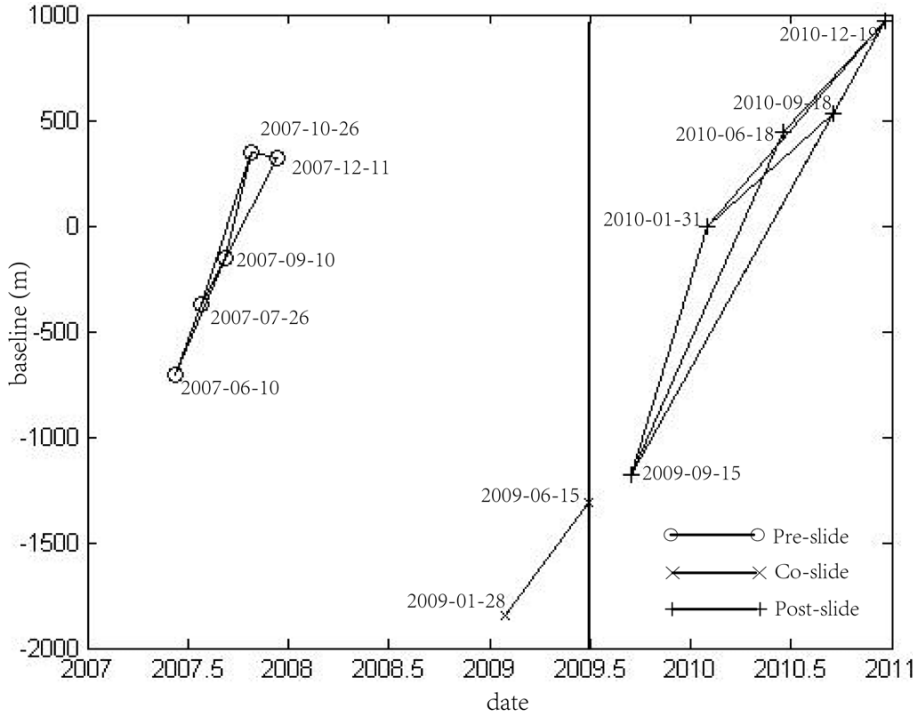

Fig. 2. Schematic figure on SAR combinations of ALOS/PALSAR imagery data for the Jiweishan rockslide analysis, different symbols indicate different SAR combinations.

NHESSD
1, 1799–1822, 2013

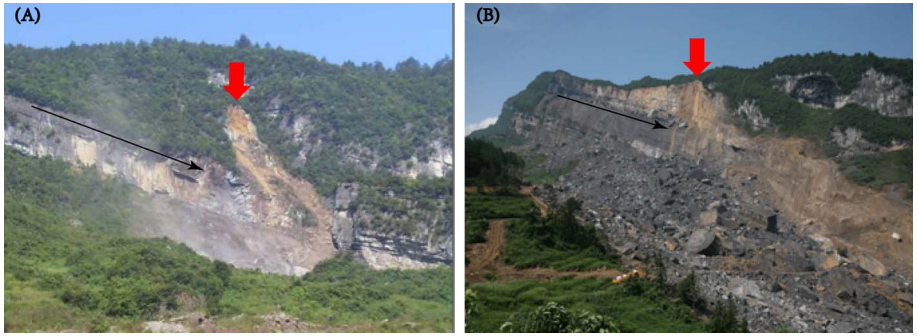

Fig. 3. Two photos over the Jiweishan rockslide, **(A)** taken 5 h before sliding and **(B)** taken after the sliding. Red arrows indicate the same location, while black arrows indicate the down-slope directions in different photos.

NHESSD
1, 1799–1822, 2013

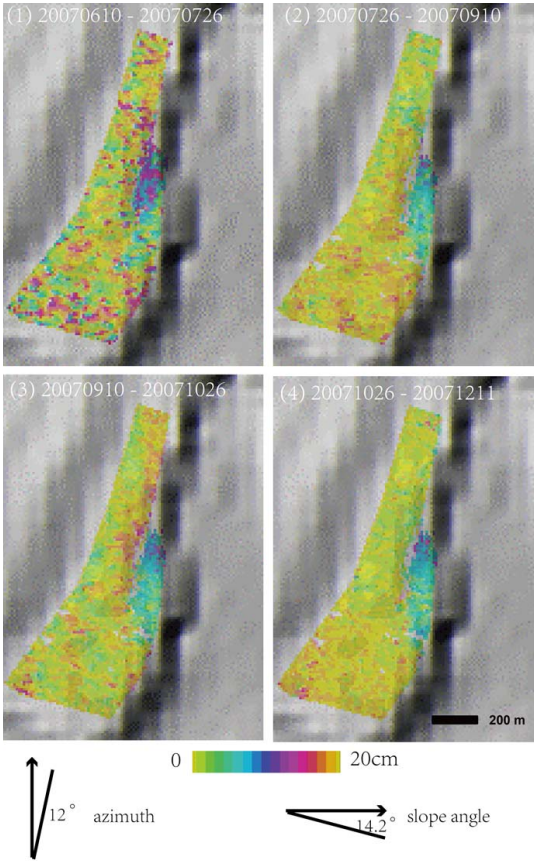

Fig. 4. Deformation maps within 46 days over the Jiweishan region before 5 June 2009 sliding. The slide geometry is shown at the bottom of the figure.

NHESSD
1, 1799–1822, 2013

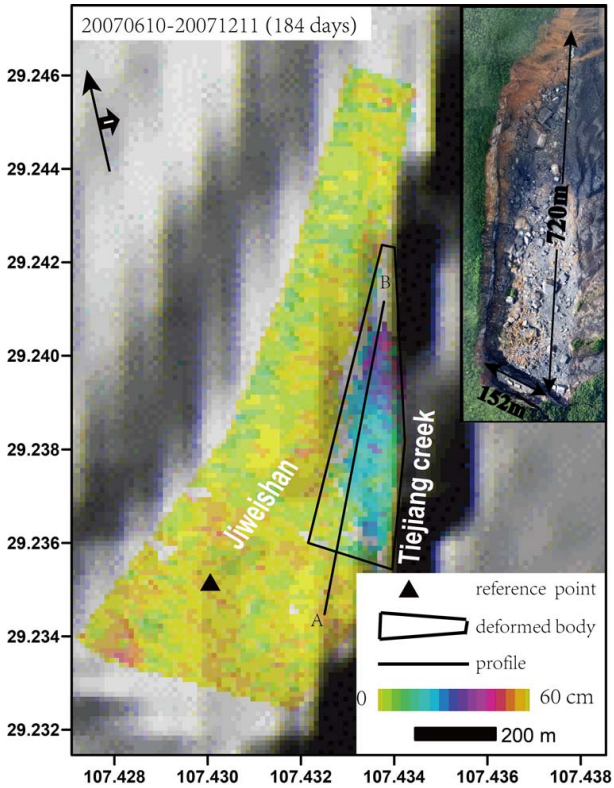

Fig. 5. The cumulative deformation map during 10 June and 11 December 2007 (184 days). The irregular polygon outlines the deformed rockslide body. Black triangle indicates the reference point for InSAR time-series analysis. Profile AB will be discussed in Fig. 6. The inset is the aerial photograph taken after Jiweishan sliding (Yin et al., 2011).

NHESSD
1, 1799–1822, 2013

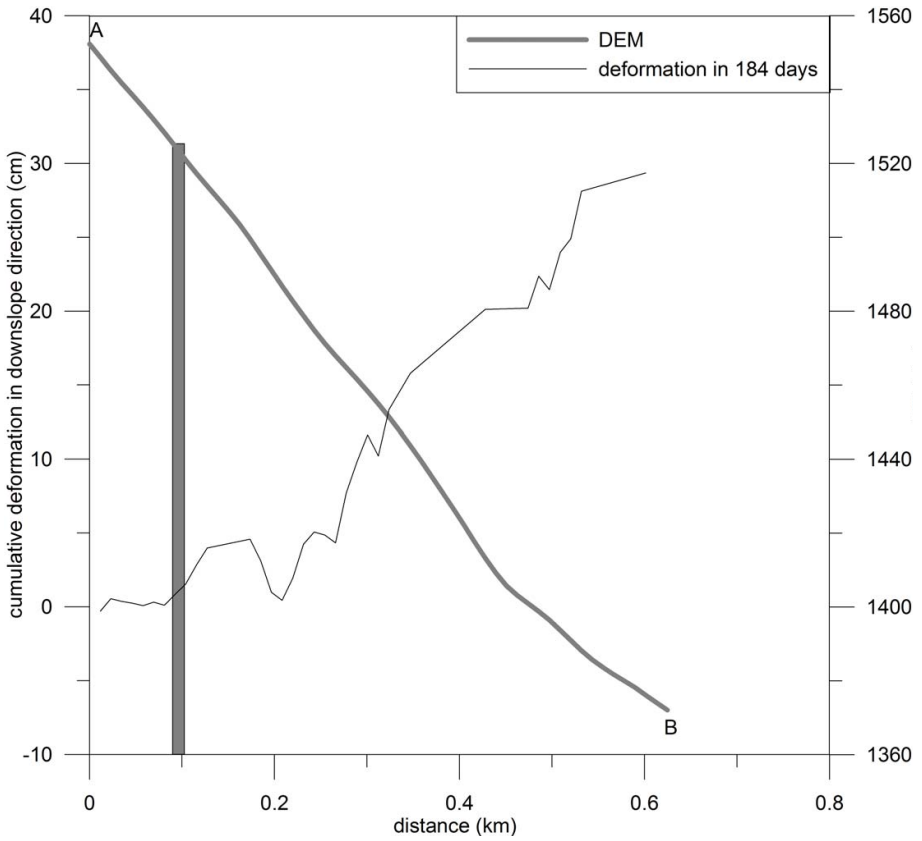

Fig. 6. Cumulative deformation in downslope direction within 184 days and SRTM DEM along profile AB shown in Fig. 5. The vertical grey bar indicates the back scarp point.

NHESSD
1, 1799–1822, 2013

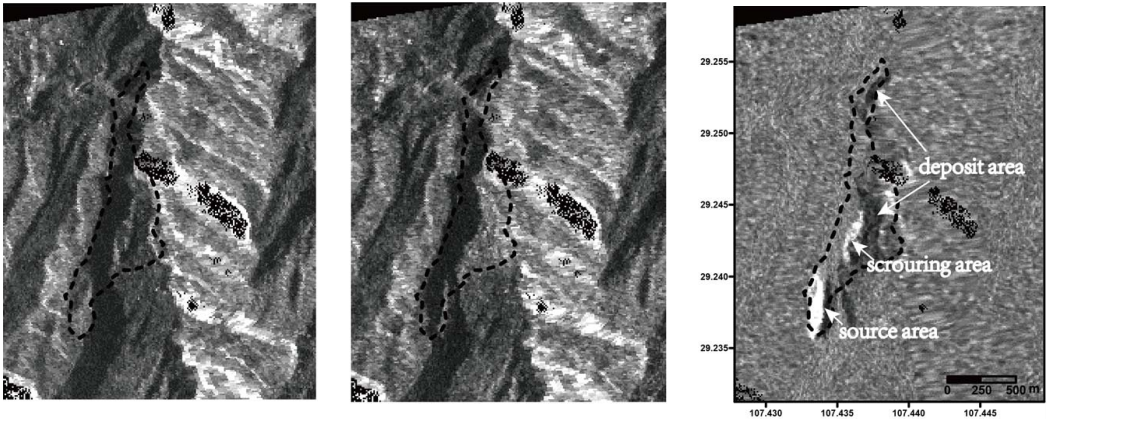

(a) intensity map in 20090128 **(b)** intensity map in 20090615 **(c)** intensity change map between **(a)** and **(b)**

Fig. 7. Two SAR Intensity images acquired on 28 January 2009 **(a)** and 15 June 2009 **(b)**. **(c)** Intensity change map between **(a)** and **(b)**. Dashed polygon is superimposed on each map to indicate the affected area inferred from aerial photo. In **(c)**, source area, scouring area and two deposit areas are indicated.

NHESSD
1, 1799–1822, 2013

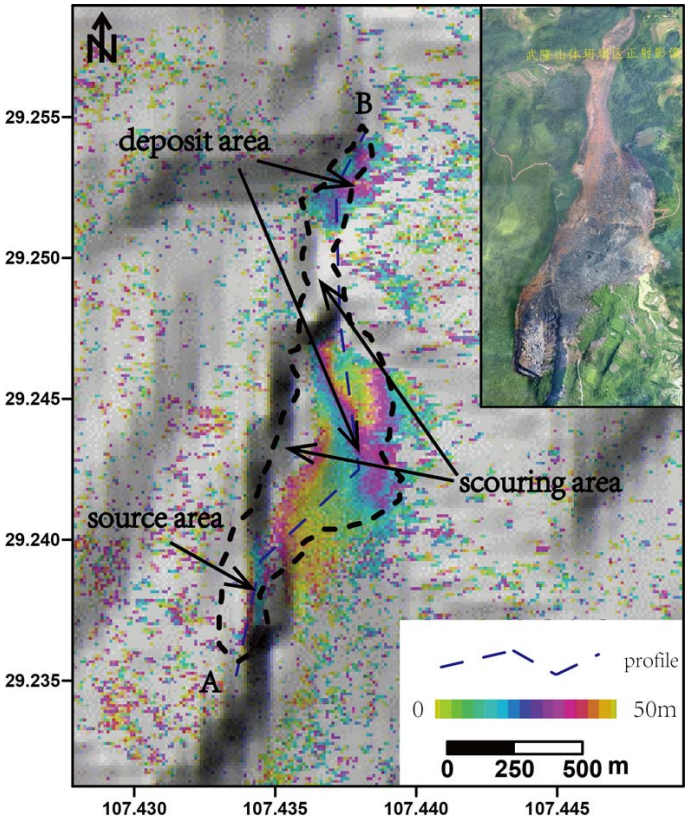

Fig. 8. DEM change map calculated by InSAR stacking method after Jiweishan sliding. The black dashed line delineates the affected region based on an aerial photo and the blue dashed line represents the location of the profile AB shown in Fig. 9.

NHESSD
1, 1799–1822, 2013

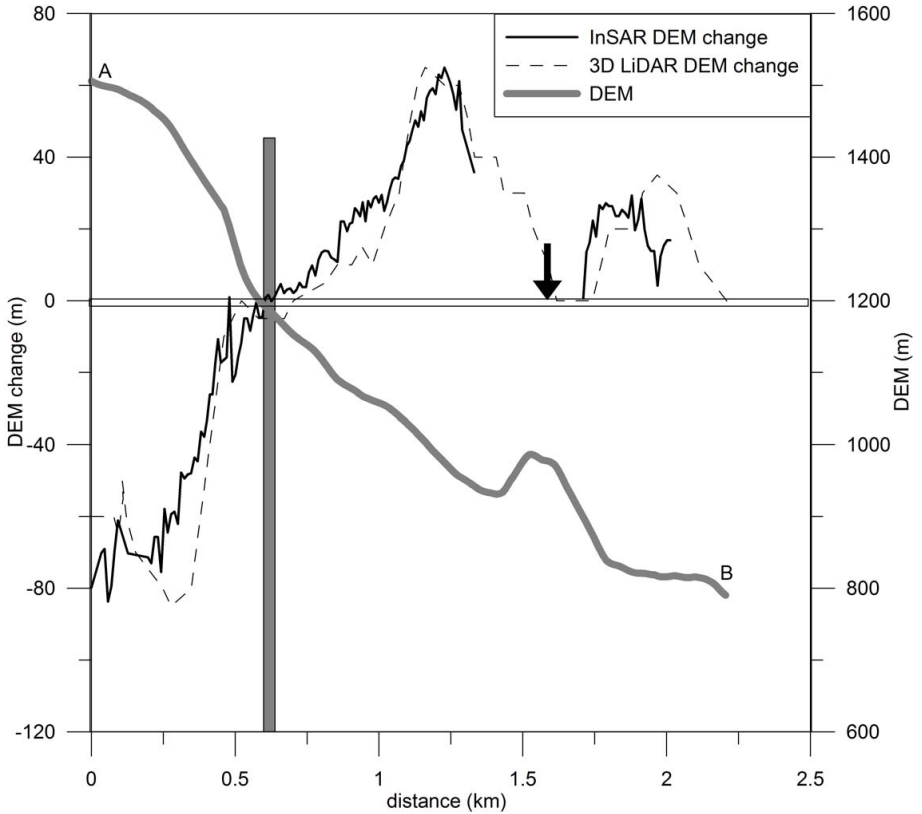

Fig. 9. Cross-section of pre-slide SRTM DEM, DEM change measured by InSAR and 3-D LiDAR techniques after Jiweishan sliding along profile AB. The vertical grey bar indicates the transaction point between the source area and the deposit area, while the black arrow shows the location of scouring region between two deposit areas.

NHESSD
1, 1799–1822, 2013